

# Observation of spin-polarized bands and domain-dependent Fermi arcs in polar Weyl semimetal MoTe<sub>2</sub>

M. Sakano<sup>1,2</sup>, M. S. Bahramy<sup>1,3</sup>, H. Tsuji<sup>1</sup>, I. Araya<sup>1</sup>, K. Ikeura<sup>1</sup>, H. Sakai<sup>1,4</sup>, S. Ishiwata<sup>1,5</sup>, K. Yaji<sup>2</sup>, K. Kuroda<sup>2</sup>, A. Harasawa<sup>2</sup>, S. Shin<sup>2</sup>, and K. Ishizaka<sup>1,3</sup>

<sup>1</sup>*Quantum-Phase Electronics Center (QPEC) and Department of Applied Physics,  
The University of Tokyo, Tokyo 113-8656, Japan*

<sup>2</sup>*Institute for Solid State Physics, The University of Tokyo, Kashiwa, Chiba 277-8581,  
Japan*

<sup>3</sup>*RIKEN Center for Emergent Matter Science (CEMS), Wako 351-0198, Japan*

<sup>4</sup>*Department of Physics, Osaka University, Toyonaka, Osaka 560-0043, Japan*

<sup>5</sup>*PRESTO, Japan Science and Technology Agency (JST), Tokyo 102-8666, Japan*

## Abstract

We investigate the surface electronic structures of 1T'-MoTe<sub>2</sub>, the Weyl semimetal candidate realized through the nonpolar-polar structural phase transition, by utilizing the laser angle-resolved photoemission spectroscopy (ARPES) combined with first-principles calculations. Two kinds of domains with different surface band dispersions are observed from a single-crystalline sample. The spin-resolved measurements further reveal that the spin polarizations of the surface and the bulk-derived states show the different domain-dependences, indicating the opposite bulk polarity. For both domains, some segment-like band features resembling the Fermi arcs are clearly observed. The patterns of the arcs present the marked contrast between the two domains, respectively agreeing well with the slab calculation of (0 0 1) and (0 0 -1) surfaces. The present result strongly suggests that the Fermi arc connects the identical pair of Weyl nodes on one side of the polar crystal surface, whereas it connects between the different pairs of Weyl nodes on the other side.

There has been increasing interest in Weyl semimetals as a new class of the topological state of matter, where the nondegenerate bands form pairs of band crossings (i.e. Weyl nodes) at the Fermi level ( $E_F$ ). The bulk electronic structure of Weyl semimetals are characterized by the spin polarized Weyl cone dispersions formed through the breaking of either time-reversal or space-inversion symmetry [1-4]. At the surface, on the other hand, the chiral charge associated with the Weyl nodes warrants the existence of the gapless surface states, so-called Fermi arcs that connect the two-dimensionally (2D) projected Weyl nodes. Due to these unusual bulk and surface electronic states, a variety of new magnetoelectric phenomena have been predicted [4-9]. Until now, several experimental verification of realistic Weyl semimetal compounds are raised by angle-resolved photoemission spectroscopy (ARPES). For the transition-metal monpnictide family (eg. TaAs [10-12]) and YbMnBi<sub>2</sub> [13], respectively the candidates of noncentrosymmetric and magnetic Weyl semimetals, the observations of Weyl cones and Fermi arcs are being reported in a past year. The further pursuit for the new class of materials is important for realizing the novel quantum phenomena arising in Weyl semimetals.

1T'-MoTe<sub>2</sub> investigated in this work is known as a semimetal [14], as experimentally confirmed in the related 1T'-WTe<sub>2</sub> [15, 16]. It shows a structural transition from monoclinic ( $P2_1/m$ ) to orthorhombic ( $Pnm2_1$ ) on cooling through 250 K [17], which accompanies the nonpolar-polar transition. Consequently, 1T'-MoTe<sub>2</sub> is classified as an unusual polar ("ferroelectric" in a broad sense) semimetal with the polarization along the stacking direction ( $c$ -axis). This peculiar structural phase transition is recently found to be related to the appearance of the superconductivity [18] as well as the critical enhancement of Seebeck effect [19, 20], thus indicating its potential influence on the anomalous electronic properties. At the same time, theoretical studies claim that the polar phase of MoTe<sub>2</sub> and WTe<sub>2</sub> are the new candidate of noncentrosymmetric type-II Weyl semimetals with two pairs of Weyl nodes, W1 and W2, where the nodes appear as the intersections of the electron and hole Fermi surfaces [21-24]. A number of recent ARPES studies also suggest that the type-II Weyl semimetal is indeed realized in MoTe<sub>2</sub> [25-31]. Nevertheless, the quantitative correspondence of Weyl nodes obtained experimentally and theoretically is still controversial, partly because of their possible sensitivity to the subtle change of atomic positions [22]. The clear comparison of Fermi arcs for top and bottom surfaces, in the light of their connectivity, is also yet unsatisfactory.

In this Letter, we investigate the electronic structures of 1T'-MoTe<sub>2</sub> by means of high-

resolution laser angle-resolved photoemission spectroscopy (ARPES). The spin polarization of the surface and bulk-derived bands for respective domains are also confirmed by the spin-resolved laser ARPES (laser-SARPES). By raising the temperature to 100 K, we successfully find the signature of Fermi arcs that reside about 30 meV above  $E_F$ . The results are in good agreement with the band calculation, and indicate that the Fermi arcs connect the identical pair of W1 nodes at (0 0 -1) surface whereas they connect the different pairs of the W1 and W2 nodes at (0 0 1) surface.

The single crystals of 1T'-MoTe<sub>2</sub> are synthesized by the chemical vapor transport method [19, 20]. ARPES at 25 K were performed using the He-discharge lamp (21.2 eV) and the fourth harmonic generation of Ti:Sapphire laser (6.43 eV, *s*-polarized light) [32], with a VG-Scienta R4000WAL analyzer. The total energy resolution was set to 10 meV and 3 meV, respectively. For the laser-SARPES at 25 K and the ARPES at 100 K, the 6.99 eV laser (*s*-polarized light) and a ScientaOmicron DA30L analyzer mounted with two sets of VLEED (very low energy electron diffraction) spin detectors were used at the Institute of Solid State Physics (ISSP), The University of Tokyo [33]. The total energy resolution was set to 30 meV and 3 meV, respectively. Samples were cleaved *in situ* at room temperature. All measurements were performed in ultrahigh vacuum better than  $1 \times 10^{-10}$  Torr. Electronic structure calculations were performed within the context of density functional theory (DFT) using the Perdew–Burke–Ernzerhof exchange–correlation functional as implemented in the VASP program [34, 35]. Relativistic effects, including spin–orbit coupling, were fully included. The structure parameter in Ref. [22] were used, and the corresponding Brillouin zone was sampled by a  $20 \times 10 \times 5$  k-mesh. For the orbital and layer projection calculation, a tight binding supercell containing 80 layers of MoTe<sub>2</sub> was constructed by downfolding the DFT results using maximally localized Wannier functions [36], employing Mo 4d orbitals and Te 5p orbitals as the projection centers.

Figure 1 shows the band structures obtained by ARPES and the calculations. The Brillouin zone for the low temperature orthorhombic structure is depicted in Fig. 1(a) with the momentum axes ( $k_x, k_y, k_z$ ). The ARPES image obtained by the HeI $\alpha$  (21.2 eV) photon is shown in Fig. 1(c). Along  $\Gamma$ -X, the complicated hybridization of bands forming the semimetallic hole and electron pockets are recognized near  $E_F$ , whereas rather simple holelike band dispersions are observed along  $\Gamma$ -Y. The band calculations along  $\Gamma$ -X focusing on the near- $E_F$  semimetallic bands are shown in Figs. 1(f) and 1(g), respectively, for the monoclinic (non-polar) high-temperature

and the orthorhombic (polar) low-temperature phases. In the low-temperature phase, due to the polarity along the stacking direction ( $c$ -axis), the spin-splitting of the bands occurs *via* the spin-orbit coupling (see the regions surrounded by the green broken curves) [37]. These spin-polarized bands can be regarded as the hallmark of the polar semimetal state that is responsible for producing the Weyl nodes located at  $E - E_F = 6$  meV (W1) and 59 meV (W2) at  $(k_x, k_y, k_z) = (0.185, 0.013, 0)$  and  $(0.181, 0.053, 0)$   $\text{\AA}^{-1}$  as reported in Ref. [22].

To focus on the near- $E_F$  electronic structure, the ARPES images along  $\Gamma$ -X recorded by using the 6.43 eV laser are shown in Figs. 1(d) and 1(e). Owing to the small spot size ( $120 \mu\text{m} \times 100 \mu\text{m}$ ), we always find two-types of domains [Surfaces A and B, respectively shown in Figs. 1(d) and 1(e)], by surveying the positions on the sample surface [see Fig. 1(b)]. In the present study, we assign these as the polar domains with the opposite bulk polarity generated through the structural transition (*vide infra*). By comparing with the slab calculations in Figs. 1(h) and 1(i), we can recognize the rather flat surface band (S1, green curve). It is located at around  $E - E_F = -80$  meV ( $-50$  meV) for Surface A (B), which merges with the bulk hole band at  $k_x \sim 0.2$   $\text{\AA}^{-1}$ . The other surface band (S2, red curve) has a dispersive character which crosses with the S1 bands. These S1 and S2 seem to connect the bulk electron and hole pockets, indicating their topologically protected nature. The band features reflecting the bulk electron pocket (brown curves), on the other hand, are similarly observed in Surfaces A and B. From this viewpoint, the slab calculations for (0 0 1) and (0 0 -1) surfaces, as shown in Figs. 1(h) and 1(i), seem to show qualitatively good agreements with the bands observed for Surface A and B, respectively [38]. By taking advantage of these domains, the termination dependence of the topological Weyl state can be investigated.

Here we use the laser-SARPES (6.99 eV) to finely resolve the spin polarized band structures along  $k_x$ , as shown in Fig. 2. The ARPES intensities of spin-up and spin-down for  $y$ -spin ( $s_y$ ) component are plotted in Figs. 2(c) and 2(d), respectively. They show marked differences, indicating that there are multiple bands with the opposite  $s_y$  polarizations. The energy distribution curves for  $s_y$ -up (red) and  $s_y$ -down (blue) are displayed in Fig. 2(e), with the peak positions also depicted by markers of the same color. By plotting these peaks, as shown in Figs. 2(c) and 2(d), we can trace the band dispersions with respective spin polarizations. The guides for these spin-polarized bands are overlaid on the high  $k$ -resolution laser (6.43 eV) ARPES image in Fig. 2(b). Here the red / pink curves indicate the bands with  $s_y$ -up components whereas the blue curves represent those with  $s_y$ -down. From this result, we can safely assign that the S1 (S2) surface state has the  $s_y$ -up ( $s_y$ -down) polarization. We also note that there is some characteristic near- $E_F$  intensity with  $s_y$ -up polarization observed at around  $k_x = 0.25 - 0.3$   $\text{\AA}^{-1}$  (detector angle  $\theta = 1 - 5$

deg.), depicted by the light blue curves and  $\circ$  markers in Figs. 2(a) and 2(e).

The results for Surface B are similarly shown in Figs. 2(f)-2(j). By comparing with Surface A, we can derive several features regarding the spin-polarized bands. The surface states S1 and S2 apparently have the same spin polarization for both surfaces, whereas the near- $E_F$  intensity has the opposite spin polarization ( $s_y$ -down for Surface A and  $s_y$ -up for Surface B). Here we note that the spin polarization for the bulk bands which split by the spin-orbit coupling, as presented in Fig. 2(g), should be opposite when we compare the polar domains. Taking these into account, we assign the bands depicted by light blue and pink  $\circ$  markers and curves in Figs. 2(e,j) and Figs. 2(a,f), respectively, as those derived from the bulk band components. These arguments, with the help of the slab calculations, strongly suggest that Surfaces A and B should correspond to the (0 0 1) and (0 0 -1) surfaces, respectively.

To seek for the possible Fermi arcs connecting the Weyl nodes located off the  $\Gamma$ -X line, we measured the energy contours for Surfaces A (0 0 1) and B (0 0 -1), as respectively shown in Figs. 3(a)-3(d) and 3(e)-3(h). The high  $k$ -resolution data at  $E_F$ , recorded at 25 K with 6.43 eV laser, present some clear differences for respective surfaces [Figs. 3(a) and 3(e)]. For Surface A (0 0 1), we observe a pair of segment-like features [indicated by the blue markers in Fig. 3(e)] touching the circular contour surrounding the bulk electron pocket, whereas no such clear segments are recognized for Surface B (0 0 -1) [Fig. 3(a)]. The pair of segments observed in Surface A (0 0 1) may be the tails of the Fermi arcs connecting W1 and W2 nodes, as predicted in the previous calculations [22]. To get closer to the W1 node in energy ( $E = E_F + 6.7$  meV), we performed the measurement at 100 K with 6.99 eV laser. Owing to the thermal excitation of electrons obeying the Fermi-Dirac distribution function, we can detect the electrons up to 30 meV above  $E_F$ , as shown in Figs. 3(b-d) and 3(f-h). At  $E - E_F = 30$ meV [Fig. 3(d)], we find a segment-like feature in Surface B (0 0 -1) that is centered at  $k_y = 0$  (indicated by the blue marker), which makes a clear contrast to the one observed in Surface A (0 0 1). The segment observed for Surface B (0 0 -1) seems to well correspond to the Fermi arc connecting the pair of W1 nodes across the  $\Gamma$ -X line, in contrast to those connecting W1 and W2 nodes in Surface A (0 0 1). This difference for respective surfaces are also well reproduced in the slab calculations as shown in Figs. 3(i)-3(k) and 3(m)-3(o), respectively. The schematic of the energy contours at W1 ( $E_F + 6.7$  meV) are indicated in Figs. 3(l) and 3(p), where the brown shaded areas represent the 2D projected bulk bands and the blue curves indicate the surface states [39].

Since W1 and W2 nodes have the very close  $k_x$  values ( $k_x \sim 0.19 \text{ \AA}^{-1}$ ) in the present case, the constant- $k_x$  (i.e.  $E$  vs  $k_y$  plane) is a good cut to show the dispersion relations of the multiple

Weyl cones and related Fermi arcs. The  $E$ - $k_y$  ARPES images for Surfaces A (0 0 1) and B (0 0 -1) recorded at 100 K are shown in Figs. 4(b) and 4(e), respectively. The positions of  $k_x$  are indicated by the blue broken lines in Figs. 4(a) and 4(d). By looking at the ARPES images divided by the Fermi-Dirac distribution function of 100 K, we see a clear contrast between the two surfaces. For Surface B (0 0 -1), there is a high intensity region at  $E - E_F > 30\text{meV}$ ,  $k_y \sim 0$ , indicated by the blue broken curve. This should correspond to the Fermi arc centered at  $k_y = 0$  connecting two W1 nodes, as shown in the calculated image in Fig. 4(c). For Surface A (0 0 1), on the other hand, there are symmetric dispersions appearing above the Fermi level at around  $k_y \sim 0.05 \text{ \AA}^{-1}$  (blue broken curves). They should be the signatures of the disconnected Fermi arcs connecting W1 and W2 nodes. These dispersions of the Fermi arcs are also well presented in the slab calculation in Fig. 4(f).

The present results thus strongly suggest that the surface-orientation dependent Fermi arcs indeed realized in the polar Weyl semimetal  $\text{MoTe}_2$ . In general, polar materials can accompany the termination-dependent surface band dispersions either generated by the bulk polarization or surface discontinuity [40, 41]. Focusing on polar Weyl semimetals, the different patterns of Fermi arcs on top and bottom surfaces are also theoretically expected [42, 43]. Indeed, an ARPES study on NbP [44] revealed the nonequivalent forms of Fermi arcs on the respective surfaces, which seems to be terminated at the same 2D projected bulk Weyl nodes. The present result on  $\text{MoTe}_2$  similarly indicates the different connectivity of the Fermi arcs to the two kinds of Weyl nodes for (0 0 1) and (0 0 -1) terminated surfaces, as predicted in Ref. [42]. However, an additional Fermi arc connecting the pair of W2 nodes on Surface B (0 0 -1) should exist in order to consistently connect the Weyl nodes. Since W2 nodes are expected to reside at 59 meV above  $E_F$  which is hardly accessible at  $< 200 \text{ K}$ , more direct investigation of the unoccupied state should be required to fully understand the whole picture of the Fermi arcs [25].

In conclusion, the laser (spin-resolved) ARPES study on  $1T'$ - $\text{MoTe}_2$  revealed the two kinds of domains with the different surface band dispersions. The spin polarizations of these surfaces states and the bulk-derived electronic structures showed the different domain-dependences, indicating that they are derived from the opposite bulk polarity of the crystal structure. We further found that the signature of Fermi arcs appearing in the ARPES energy contours possess the nonequivalent forms for the both domains, respectively connecting the identical pair of W1 nodes (domain B) and the different pairs of W1 and W2 nodes (domain A). They agree well with the slab calculations on (0 0 -1) and (0 0 1) surfaces, respectively. The present results demonstrate a credible support for the type-II Weyl semimetal state realized in the

polar  $1T^{\prime}$ -MoTe<sub>2</sub>.

#### Acknowledgement

This research was partly supported by the Photon Frontier Network Program of the MEXT; Research Hub for Advanced Nano Characterization, The University of Tokyo, supported by MEXT, Japan; and Grant-in-Aid for Scientific Research from JSPS, Japan (KAKENHI 15H03683 and 16K133815).

## Reference

1. S. Murakami, *New J. of Phys.* **9**, 356 (2007).
2. X. Wan, A. M. Turner, A. Vishwanath, and S. Y. Savrasov, *Phys. Rev. B* **83**, 205101 (2011).
3. A. A. Burkov and L. Balents, *Phys. Rev. Lett.* **107**, 127205 (2011).
4. G. Xu, H. Weng, Z. Wang, X. Dai, and Z. Fang, *Phys. Rev. Lett.* **107**, 186806 (2011).
5. H. B. Nielsen and M. Ninomiya, *Phys. Lett. B* **130**, 389 (1983).
6. A. A. Zyuzin and A. A. Burkov, *Phys. Rev. B* **86**, 115133 (2012).
7. Z. Wang and S.-C. Zhang, *Phys. Rev. B* **87**, 161107(R) (2013).
8. M. M. Vazifeh and M. Franz, *Phys. Rev. Lett.* **111**, 027201 (2013).
9. A. A. Burkov, *J. Phys.: Condens. Matter* **27**, 113201 (2015).
10. S.-Y. Xu, I. Belopolski, N. Alidoust, M. Neupane, G. Bian, C. Zhang, R. Sankar, G. Chang, Z. Yuan, C.-C. Lee, S.-M. Huang, H. Zheng, J. Ma, D. S. Sanchez, B. Wang, A. Bansil, F. Chou, P. P. Shibayev, H. Lin, S. Jia, and M. Z. Hasan, *Science* **349**, 613 (2015).
11. B. Q. Lv, H. M. Weng, B. B. Fu, X. P. Wang, H. Miao, J. Ma, P. Richard, X. C. Huang, L. X. Zhao, G. F. Chen, Z. Fang, X. Dai, T. Qian, and H. Ding, *Phys. Rev. X* **5**, 031013 (2015).
12. L. X. Yang, Z. K. Liu, Y. Sun, H. Peng, H. F. Yang, T. Zhang, B. Zhou, Y. Zhang, Y. F. Guo, M. Rahn, D. Prabhakaran, Z. Hussain, S.-K. Mo, C. Felser, B. Yan, and Y. L. Chen, *Nat. Phys.* **11**, 728-732 (2015).
13. S. Borisenko, D. Evtushinsky, Q. Gibson, A. Yaresko, T. Kim, M. N. Ali, B. Büchner, M. Hoesch, R. J. Cava, arXiv:1507.04847.
14. W. G. Dawson and D. W. Bullett, *J. Phys. C: Solid State Phys.* **2**, 6159 (1987).
15. I. Pletikosić, Mazhar N. Ali, A. V. Fedorov, R. J. Cava and T. Valla, *Phys. Rev. Lett.* **113**, 216601 (2014).
16. Y. Wu, N. H. Jo, M. Ochi, L. Huang, D. Mou, S. L. Bud'ko, P. C. Canfield, N. Trivedi, R. Arita and A. Kaminski, *Phys. Rev. Lett* **115**, 166602 (2015).
17. R. Clarke, E. Marseglia, and H. P. Hughes, *Phil. Mag.* **38**, 121 (1978).
18. Y. Qi, P. G. Naumov, M. N. Ali, C. R. Rajamathi, Y. Sun, C. Shekhar, S.-C. Wu, V. S üß, M. Schmidt, E. Pippel, P. Werner, R. Hillebrand, T. Forster, E. Kampertt, W. Schnelle,

- S. Parkin, R. J. Cava, C. Felser, B. Yan, and S. A. Medvedev, *Nat. Commun.* **7**, 11038 (2016).
19. K. Ikeura, H. Sakai, M. S. Bahramy, and S. Ishiwata, *APL Materials.* **3**, 041514 (2015).
  20. H. Sakai, K. Ikeura, M. S. Bahramy, N. Ogawa, D. Hashizume, J. Fujioka, Y. Tokura, and S. Ishiwata, *Sci. Adv.* (in press).
  21. A. A. Soluyanov, D. Gresch, Z. Wang, Q. S. Wu, M. Troyer, X. Dai, and B. A. Bernevig, *Nature* **527**, 495 (2015).
  22. Y. Sun, S.-C. Wu, M. N. Ali, C. Felser, and B. Yan, *Phys. Rev. B* **92**, 161107(R) (2015).
  23. T.-R. Chang, S.-Y. Xu, G. Chang, C.-C. Lee, S.-M. Huang, B. Wang, G. Bian, H. Zheng, D. S. Sanchez, I. Belopolski, N. Alidoust, M. Neupane, A. Bansil, H.-T. Jeng, H. Lin and M. Z. Hasan, *Nat. Commun.* **7**, 10639 (2016).
  24. Z. Wang, D. Gresch, A. A. Soluyanov, W. Xie, S. Kushwaha, X. Dai, M. Troyer, R. J. Cava, and B. A. Bernevig, *Phys. Rev. Lett.* **117**, 056805 (2016).
  25. I. Belopolski, S.-Y. Xu, Y. Ishida, X. Pan, P. Yu, D. S. Sanchez, M. Neupane, N. Alidoust, G. Chang, T.-R. Chang, Y. Wu, G. Bian, S.-M. Huang, C.-C. Lee, D. Mou, L. Huang, Y. Song, B. Wang, G. Wang, Y.-W. Yeh, N. Yao, J. E. Rault, P. Le Fevre, F. Bertran, H.-T. Jeng, T. Kondo, A. Kaminski, H. Lin, Z. Liu, F. Song, S. Shin, and M. Z. Hasan, Fermi arc electronic structure and Chern numbers in the type-II Weyl semimetal candidate  $\text{Mo}_x\text{W}_{1-x}\text{Te}_2$ , *Phys. Rev. B* **94**, 085127 (2014).
  26. L. Huang, T. M. McCormick, M. Ochi, M.-T. Suzuki, R. Arita, Y. Wu, D. Mou, H. Cao, J. Yan, N. Trivedi, and A. Kaminski, Spectroscopic evidence for type II Weyl semimetallic state in  $\text{MoTe}_2$ , *Nat. Mater.* **15**, 1155-1160 (2016).
  27. K. Deng, G. Wan, P. Deng, K. Zhang, S. Ding, E. Wang, M. Yan, H. Huang, H. Zhang, Z. Xu, J. Denlinger, A. Fedorov, H. Yang, W. Duan, H. Yao, Y. Wu, Y. S. Fan, H. Zhang, X. Chen, and S. Zhou, Experimental observation of topological Fermi arcs in type-II Weyl semimetal  $\text{MoTe}_2$ , arXiv:1603.08508.
  28. J. Jiang, Z. K. Liu, Y. Sun, H. F. Yang, R. Rajamathi, Y. P. Qi, C. Yang, L. X. adn Chen, H. Peng, C.-C. Hwang, S. Z. Sun, M. S.-K., I. Vobornik, J. Fujii, S. S. P. Parkin, C. Felser, B. H. Yan, and Y. L. Chen, Observation of the Type-II Weyl Semimetal Phase in  $\text{MoTe}_2$ , arXiv:1604.00139.

29. A. Liang, J. Huang, S. Nie, Y. Ding, Q. Gao, C. Hu, S. He, Y. Zhang, C. Wang, B. Shen, J. Liu, P. Ai, L. Yu, X. Sun, W. Zhao, S. Lv, D. Liu, C. Li, Y. Zhang, Y. Hu, Y. Xu, L. Zhao, G. Liu, Z. Mao, X. Jia, F. Zhang, S. Zhang, F. Yang, Z. Wang, Q. Peng, H. Weng, X. Dai, Z. Fang, Z. Xu, C. Chen, and X. J. Zhou, Electronic Evidence for Type II Weyl Semimetal State in MoTe<sub>2</sub>, arXiv:1604.01706.
30. N. Xu, Z. J. Wang, A. P. Weber, A. Magrez, P. Bugnon, H. Berger, B. B. Fu, B. Q. Lv, N. C. Plumb, M. Radovic, K. Conder, T. Qian, J. H. Dil, J. Mesot, H. Ding, and M. Shi, Discovery of Weyl semimetal state violating Lorentz invariance in MoTe<sub>2</sub>, arXiv:1604.02116.
31. A. Tamai, Q. S. Wu, I. Cucchi, F. Y. Bruno, S. Riccò, T.K. Kim, M. Hoesch, C. Barreteau, E. Giannini, C. Besnard, A. A. Soluyanov, and F. Baumberger, Fermi Arcs and Their Topological Character in the Candidate Type-II Weyl Semimetal MoTe<sub>2</sub>, Phys. Rev. X **6**, 031021(2016).
32. Y. Suzuki, T. Shimojima, T. Sonobe, A. Nakamura, M. Sakano, H. Tsuji, J. Omachi, K. Yoshioka, M. Kuwata-Gonokami, T. Watashige, R. Kobayashi, S. Kasahara, T. Shibauchi, Y. Matsuda, Y. Yamakawa, H. Kontani, and K. Ishizaka, Phys. Rev. B **92**, 205117 (2015).
33. K. Yaji, A. Harasawa, K. Kuroda, S. Toyohisa, M. Nakayama, Y. Ishida, A. Fukushima, S. Watanabe, C. Chen, F. Komori, and S. Shin, Rev. Sci. Instrum. **87**, 053111 (2016).
34. J. P. Perdew, K. Burke and M. Ernzerhof, Phys. Rev. Lett. **77**, 38653868 (1996).
35. G. Kresse *et al.*, <http://cms.mpi.univie.ac.at/vasp/> (2012).
36. A. A. Mostofi, J. R. Yates, Y. -S. Lee, D. Vanderbilt, and N. Marzari, Comput. Phys. Commun. **178**, 685 (2008).
37. K. Ishizaka, M. S. Bahramy, H. Murakawa, M. Sakano, T. Shimojima, T. Sonobe, K. Koizumi, S. Shin, H. Miyahara, A. Kimura, K. Miyamoto, T. Okuda, H. Namatame, M. Taniguchi, R. Arita, N. Nagaosa, K. Kobayashi, Y. Murakami, R. Kumai, Y. Kaneko, Y. Onose, and Y. Tokura, Nat. Mater. **10**, 521 (2011).
38. By comparing the energy of the bottom of the bulk electron pocket, we can estimate that the Fermi level for the ARPES result is about 30 meV lower as compared to the band calculation. It should be attributed to the nonstoichiometry of the single crystalline samples where the excess holes tend to be introduced by the Te deficiency [20].
39. One may notice that the W1-W1 Fermi arc in Surface A (0 0 1) appears better at higher energy ( $E > E_F + 15$  meV) whereas the W1-W2 Fermi arcs in Surface B (0 0 -1) are more

- distinguishable at lower energy ( $E < E_F + 15$  meV). It can be explained by the difference of the distributions of the Fermi arcs in the energy vs 2D momentum space. W1-W1 Fermi arc in Surface A (0 0 1) quickly disappears at the energy below the W1 nodes, by merging to the surface state of circular contour. W1-W2 Fermi arcs, on the other hand, can be seen surviving to the lower energies below  $E_F$ , thus making it easier to observe by low temperature ARPES.
40. A. Crepaldi, L. Moreschini, G. Audebert, C. Tournier-Colletta, S. Moser, N. Virk, H. Berger, Ph. Bugnon, Y. J. Chang, K. Kern, A. Bostwick, E. Rotenberg, O. V. Yazyev, and M. Grioni, *Phys. Rev. Lett.* **109**, 096803 (2012).
  41. G. Landolt, S. V. Eremeev, Y. M. Koroteev, B. Slomski, S. Muff, T. Neupert, M. Kobayashi, V. N. Strocov, T. Schmitt, Z. S. Aliev, M. B. Babanly, I. R. Amiraslanov, E. V. Chulkov, J. Osterwalder, and J. H. Dil, *Phys. Rev. Lett.* **109**, 116403 (2012).
  42. R. Okugawa and S. Murakami, *Phys. Rev. B* **89**, 235315 (2014).
  43. S.-M. Huang, S.-Y. Xu, I. Belopolski, C.-C. Lee, G. Chang, B. Wang, N. Alidoust, G. Bian, M. Neupane, A. Bansil, H. Lin and M. Z. Hasan, *Nat. Commun.* **6**, 7373 (2015).
  44. S. Souma, Zhiwei Wang, H. Kotaka, T. Sato, K. Nakayama, Y. Tanaka, H. Kimizuka, T. Takahashi, K. Yamauchi, T. Oguchi, K. Segawa, and Y. Ando, *Phys. Rev. B* **93** 161112(R) (2016).

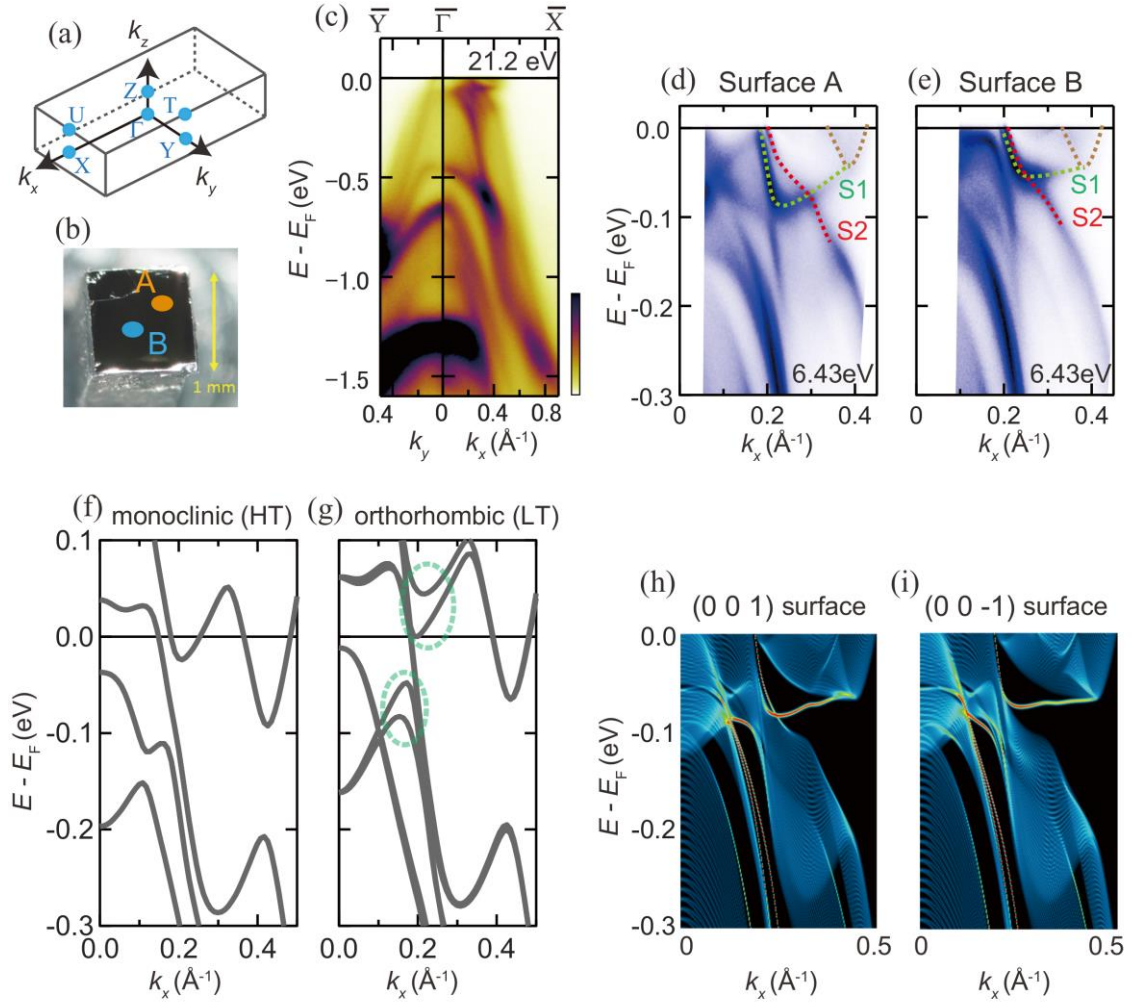


**Fig.1** (a) The Brillouin zone of orthorhombic MoTe<sub>2</sub>. (b) The typical sample of single-crystalline MoTe<sub>2</sub>. The markers A and B show the spots where the two different kinds of the surface states (namely Surface A and B) are observed. (c) ARPES image recorded at 25 K with the photon energy of 21.2 eV. (d) and (e) ARPES images along  $k_x$  axis recorded at 25 K with 6.43 eV laser, from Surfaces A and B, respectively. The green (red) broken curves indicate the S1 (S2) surface states, whereas the brown broken curves denote the bulk-derived bands. (f) and (g) The band calculations of MoTe<sub>2</sub> along  $(k_x, 0, 0)$  for high temperature (HT) monoclinic and low temperature (LT) orthorhombic structures, respectively. The green broken curves in (g) indicate the regions where the spin-splitting is induced by the polar structure. (h) and (i) The slab calculation along  $k_x$  axis for the (0 0 1) and (0 0 -1) surfaces, respectively.

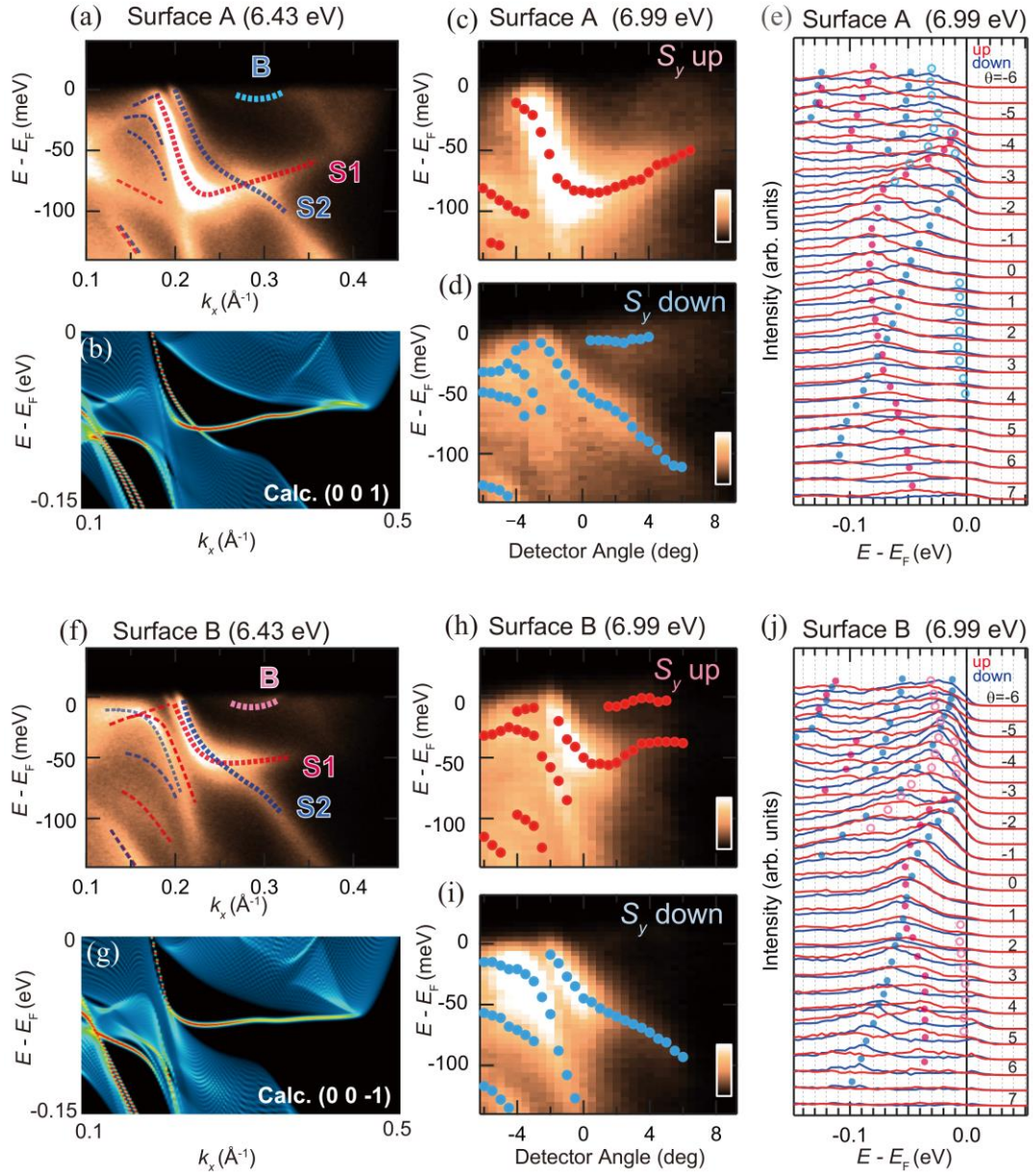


**Fig.2** (a) ARPES image along  $k_x$  axis for Surface A obtained by 6.43 eV laser. The blue (red / pink) broken curves indicate the guides for the band dispersions with  $s_y$ -down ( $s_y$ -up) polarizations. (b) The corresponding slab calculation for (0 0 1) surface. (c) and (d) Laser-SARPES images for  $s_y$ -up and  $s_y$ -down, respectively, obtained from Surface A by using 6.99 eV laser (ISSP). The detector slit is fixed along  $k_x$  axis. (e) Energy distribution curves (EDCs) for  $s_y$ -up (red) and  $s_y$ -down (blue), respectively. The markers indicate the positions of the intensity peaks, which are also plotted in (c) and (d). (f)-(j) A similar set of ARPES image, slab calculation, laser-SARPES image, and EDC data are presented for Surface B and (0 0 -1) surface.

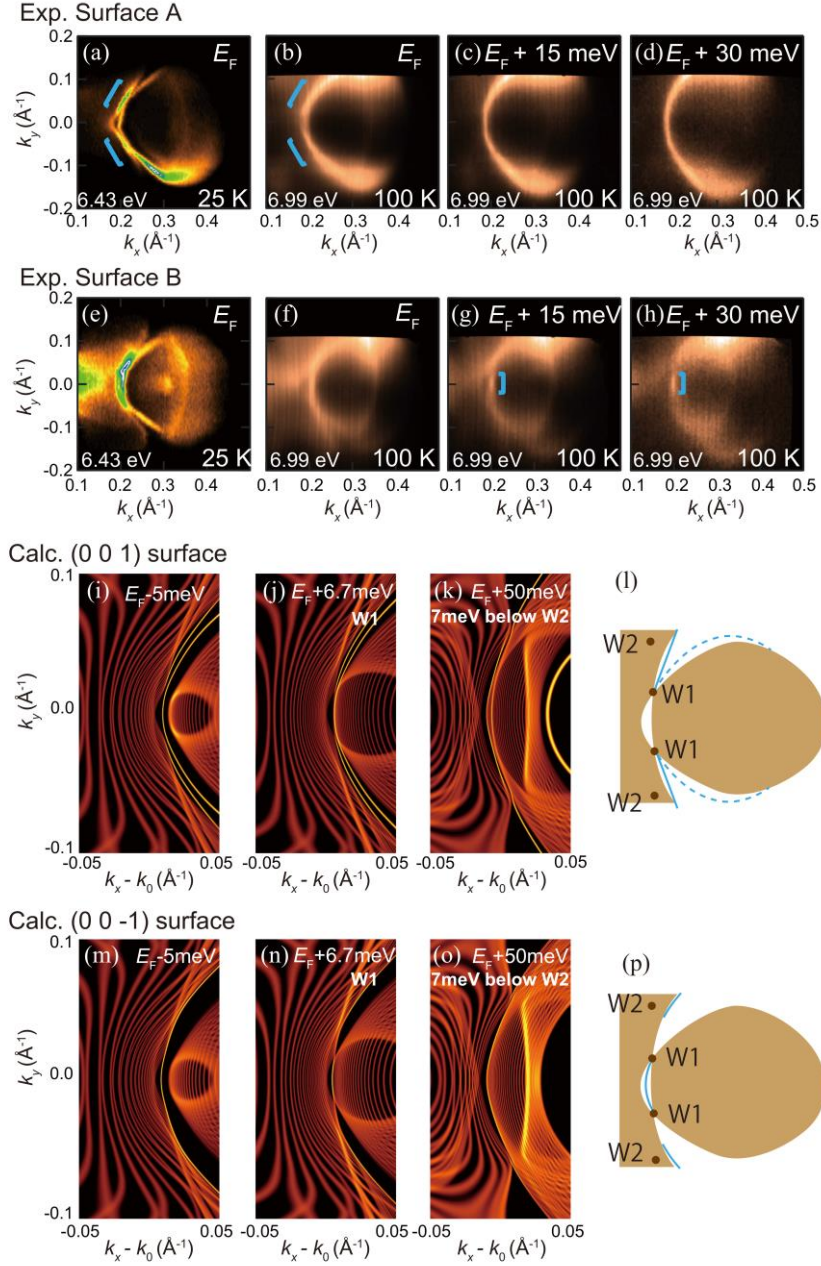


**Fig.3** The energy contours at  $E_F$  recorded at 25 K (a) and  $E_F$ ,  $E_F + 15$  meV,  $E_F + 30$  meV recorded at 100 K (b)-(d), respectively, obtained from Surface A. The similar set of energy contours from Surface B is shown in (e)-(h). The data at 25 K (100 K) are obtained using 6.43 eV laser (6.99 eV laser at ISSP). The calculated energy contours at  $E_F - 5$  meV,  $E_F + 6.7$  meV (i.e. W1), and  $E_F + 50$  meV (i.e. 7 meV below W2) are shown in (i)-(k), respectively, for (0 0 1) surface. The corresponding schematic energy contour at the W1 energy is depicted in (l), with the brown shades indicating the 2D projected bulk and the blue curves indicating the surface states. The similar set of data for (0 0 -1) surface is shown in (m)-(p).

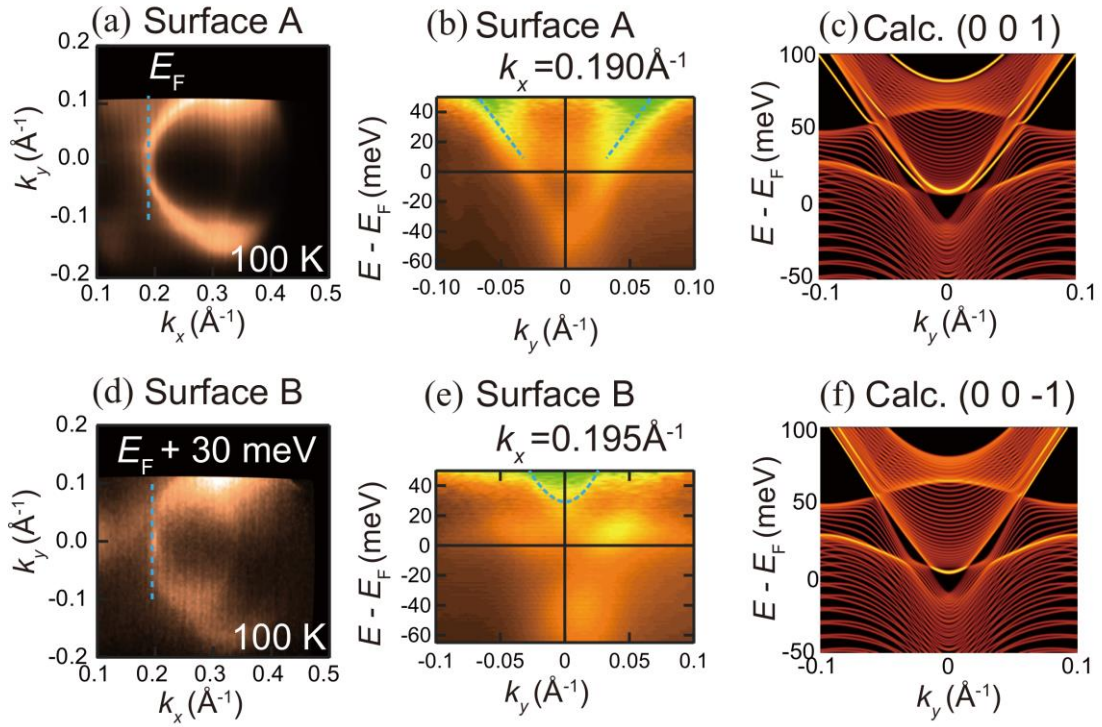


**Fig.4** The energy contour at  $E_F + 30$  meV (a) and  $E-k_y$  ARPES image divided by the Fermi Dirac distribution function at 100 K (b), and the calculated  $E-k_y$  image at  $k_x = k_0$  (c), obtained for (0 0 1) surface. The energy contour at  $E_F$  (d) and  $E-k_y$  ARPES image divided by the Fermi Dirac distribution function at 100 K (e), and the calculated  $E-k_y$  image at  $k_x = k_0$  (f), obtained for (0 0 -1) surface. The ARPES data are obtained using 6.99 eV laser at ISSP.